

Flamelet Connection to Turbulence Kinetic Energy Dissipation Rate

William A. Sirignano, Wes Hellwig, Sylvain L. Walsh

Department of Mechanical and Aerospace Engineering

University of California, Irvine, CA 92697

September 10, 2024

Abstract

An analysis takes the variable value for turbulence kinetic energy dissipation rate ϵ as it might appear from a turbulent combustion computation using either Reynolds-averaged Navier-Stokes (RANS) or large-eddy simulation (LES) and relates it to both viscous dissipation rate and turbulence kinetic energy at the Kolmogorov scale. The imposed strain rate and vorticity on these smallest eddies are readily and uniquely determined from knowledge of that kinetic energy and viscous dissipation rate. Thus, a given value of ϵ at a specific time and location determines the two mechanical constraints (vorticity and strain rate) on the inflow to the flamelet. It is also shown how ϵ affects the sign of the Laplacian of pressure, which must be negative to allow the existence of the flamelet. Using several different flamelet models, with and without vorticity and with and without differential mass transport, different results for maximum flamelet temperature, integrated flamelet burning rate, and stoichiometric flamelet scalar dissipation rate are obtained. For a given ϵ value, flamelet models that do not consider vorticity and differential diffusion produce substantial errors in the information to be provided to the resolved or filtered scales in a turbulent combustion computation.

1 Introduction

The major method for energy conversion for high levels of mechanical power and heating continues to be combustion with high mass fluxes. Inherently, the high mass-flow rate involves turbulent flow. Consequently, many physical length and time scales emerge and present challenges for both computational and experimental analyses. Large-eddy simulations (LES) are employed for computations where the smallest scales cannot be resolved. The smaller scales are filtered via integration over a window size commensurate with the computational mesh size, thereby allowing affordable computations. Consequently, the essential, rate-controlling, physical and chemical processes that occur on scales smaller than the filter size must be described by flamelet closure models. The flamelet models must handle multi-species, multi-step oxidation kinetics without requiring small time steps during the solution of the resolved-scale fluid dynamics. Thus, savings of computational resources can be huge compared to direct numerical simulation. The focus here is on the types of turbulent flames found in the shear-driven flows of practical combustors. Thereby, we address flamelets as originally described by Williams (1975), namely “highly sheared small diffusion flamelets” and “forming a turbulent flame brush which appears on the average to fill” the flow domain.

The goal here is to establish useful connections of Reynolds-averaged Navier-Stokes (RANS) and large-eddy simulation (LES) frameworks. The formulation developed here becomes a candidate for relating the resolved scale of RANS or LES to the subgrid scale for the flamelet. For the LES, we especially aim for detached-eddy simulations where, like RANS, resolutions of turbulence kinetic energy k and turbulence kinetic energy dissipation rate ϵ are determined to describe the flow below the filtered length scale.

The brief literature review of the flamelet models is presented in Section 2. A brief overview of key relations for the rotational flamelet model is given in Section 3. The description of the velocity divergence and curl in the rotating flamelet reference frame is discussed in Section 4 while the viscous dissipation, enstrophy, and kinetic energy in that frame are discussed in Sections 5 and 6. Scaling of velocity gradients between the resolved scale and flamelet level are analyzed in Section 7; specific use of and connection of the flamelet inflow with turbulence kinetic energy dissipation rate is addressed in Section 8. Results of calculations for several flamelet model forms are discussed in Section XX and Conclusions are given in Section XXX.

2 Flamelet Closure Models

It is critical to understand the laminar mixing and combustion that commonly occur within the smallest turbulent eddies. These laminar flamelet sub-domains experience significant strain of all types: shear, tensile, and compressive. Notable works exist here for either counterflows with only normal strain or simple vortex structures in two-dimensions or axisymmetry and often with a constant-density approximation. See Liñán (1974), Marble (1985), Karagozian & Marble (1986), Cetegen & Sirignano (1988), Cetegen & Sirignano (1990), Peters (2000), and Pierce & Moin (2004). An interesting review of the early flamelet theory is given by Williams (2000). Flamelet studies have focused on either premixed or nonpremixed flames; a unifying approach to premixed, nonpremixed, and multi-branched flames is needed.

Vorticity interaction with the flame has not been directly considered in most models (Liñán, 1974; Peters, 2000; Williams, 2000; Pierce & Moin, 2004). Two-dimensional planar and axisymmetric counterflow configurations are generally the foundation for a flamelet model. Local conversion to a coordinate system based on the principal strain-rate directions can provide the counterflow configuration in a general flow. Furthermore, the quasi-steady counterflow can be analyzed by ordinary differential equations because the dependence on the transverse coordinate is either constant or linear, depending on the variable. The mixture fraction has been used widely as an independent variable to display non-premixed flamelet scalar variations; this cannot be useful for premixed flames. Sirignano (2021*a*) has shown that any conserved scalar can serve well as an independent variable to present scalar results for nonpremixed and multi-branched flamelets.

Hamins *et al.* (1985) have shown through experiments and asymptotic analysis that a partially premixed fuel-lean flame and a diffusion flame can co-exist in a counterflow with opposing streams of heptane vapor and methane-oxygen-nitrogen mixture. Thus, a need exists for flamelet theory to address both premixed and non-premixed flames. Recently, Rajamanickam *et al.* (2019) provided an interesting three-dimensional triple-flame analysis, describing the effect of imposed normal strain on a multibranched flame. They did not consider shear strain, but it was followed by the work of Sirignano (2021*b*) where both shear strain and normal strain were considered. The classical counterflow treatment (Bilger, 1976; Liñán, 1974; Peters, 2000) has two opposing streams, fuel or fuel plus a chemically inert gas and oxidizer or oxidizer plus an inert gas. They considered uniform density. That critical

assumption was relaxed by (Sirignano, 2019) for reacting flows and heated flows. Sirignano (2021*a,b*) with one-step kinetics and López-Cámara *et al.* (2020) with detailed kinetics address situations where the inflowing streams consist of a combustible mixture of fuel and oxidizer, thereby allowing another flame or two besides the simple diffusion flame to co-exist. Sirignano (2021*a*) provides a counterflow analysis that shows the various permissible flame configurations pertaining to the specific compositions of the inflowing streams: (i) three flames including fuel-lean partially premixed, nonpremixed (i.e., diffusion-controlled), and fuel-rich partially premixed; (ii) nonpremixed and fuel-rich partially premixed; (iii) fuel-lean partially premixed and nonpremixed; (iv) nonpremixed; and (v) premixed. López-Cámara *et al.* (2020) extended the counterflow analysis to consider detailed kinetics for methane-oxygen detailed chemical kinetics and confirmed that combinations of premixed and non-premixed flames could exist in a multi-flame counterflow.

The effects of both normal strain rate and shear strain rate should be determined. Mixing and combustion in three-dimensional flows need to be studied with imposed normal strain and shear strain and therein imposed vorticity. Several new flamelet models have been developed for use in sub-grid closure modeling. They would be coupled with the resolved flow description for turbulent combustion. These models differ from current models in several critical ways. (i) Non-premixed flames, premixed flames, or multi-branched flame structures are determined rather than prescribed. (ii) The effects of shear strain and vorticity on the flames are determined. (iii) The strain rates and vorticity applied at the sub-grid level are directly determined from the resolved-scale strain rates and vorticity without the use of a contrived progress variable. (iv) The flamelet model is three-dimensional without need for assuming axisymmetry or planar geometry. (v) The effect of variable density is addressed in the flamelet model. Solutions to the Navier-Stokes equations and the associated scalar equations governing the flamelet model are obtained without the boundary-layer approximation.

By appropriate coordinate transformation, a similar solution is found for each flamelet model, reducing it to system of ordinary differential equations (ODEs). Sirignano (2022*c*) considers a rotational flamelet with uniform vorticity over the small flamelet domain; t2022che three-dimensional counterflow has one compressive-normal-strain direction aligned with scalar gradients and two extensional-normal-strain directions. Sirignano (2022*a*) considers a stretched vortex tube with inward swirl created by two compressive-strain directions and the extensional direction aligned with the vorticity vector.

Here, we have an analog to the classical Burgers stretched vortex (Burgers, 1948; Rott, 1958). In both models, vorticity is shown to create a centrifugal force on the sub-grid counterflow that modifies the molecular transport rates and burning rate. This has consequence on the flow rate through the flame zone and the burning rate. It thereby modifies flammability limits. Another model has been introduced Sirignano (2022*b*) where shear strain is explicitly represented in the x, y plane creating a vortex layer with counterflow in the y, z plane producing vortex stretching. This model is an analog to the Burgers vortex-layer model (Burgers, 1951; Batchelor, 1967; Robinson & Saffman, 1984). In the rotational flamelet and the stretched-vortex-tube three-dimensional models, the imposed vorticity had consequence on the scalar fields and the burning rate through the centrifugal acceleration. However, here, the vortex-layer model is asymptotically two-dimensional with no centrifugal effect, and a resulting one-way coupling between the scalar field and the vorticity; vorticity does not affect scalar profiles while the scalars can have some affect on vorticity.

The analytical frameworks allow for multi-step, detailed kinetics although the presented calculations are limited to one-step kinetics. Hellwig *et al.* (2023*a*) has recently extended the analysis to include detailed kinetics and transport and variable thermophysical properties with a more complete examination of flammability limits. The quasi-steady assumption commonly used in previous flamelet models is maintained here for the flamelet. Premixed flames can only exist with orders-of-magnitude larger values of Da compared to diffusion flamelets or multibranched flames. So, premixed flames will be less likely to survive extinction in a turbulent situation with high strain rates. The partially premixed flames in a multi-branched flame structure are driven by heat flux from the diffusion flame; thereby, they survive at lower values of Damköhler number Da . Hellwig *et al.* (2023*b*) examined the scalar dissipation-rate prediction of the rotational-flamelet model in the case where Fickian diffusion at the same rate is assumed for all species, a condition used in the Progress Variable Method, which neglected vorticity and implicitly used only a compressive normal strain rate. The rotational flamelet has the direct input of both strain rate and vorticity. For both models, it is found that a given maximum temperature or reaction rate correlates with a specific scalar dissipation rate (SDR) in the reaction zone. However, different imposed values of compressive strain rate and vorticity impose that same value of SDR.

Scaling laws have been presented (Sirignano, 2022*c*) for relating strain

rates and vorticity at the sub-grid level to those quantities at the resolved-flow level for coupling with large-eddy simulations or the time-averaged mean-flow level for Reynolds-averaged flows. The time-averaged behavior of a simple turbulent flow is resolved with coupling to the rotational flamelet model. Specifically, a two-dimensional, multicomponent, time-averaged planar shear layer with variable density and energy release is employed using a mixing-length description for the eddy viscosity.

Useful background information relevant to turbulent nonpremixed combustion is given by Elghobashi & Pun (1974); Elghobashi (1977); Nomura & Elghobashi (1992, 1993); Boratav *et al.* (1996, 1998); Ashurst *et al.* (1987); Hamlington *et al.* (2008). Background for premixed turbulent combustion is found with Driscoll *et al.* (2020); Steinberg *et al.* (2021); Steinberg & Driscoll (2009); Hamlington *et al.* (2010); Swaminathan & Grout (2006).

Here, we address the use of turbulence kinetic energy dissipation rate ϵ to connect the RANS resolved-scale or LES filtered-scale for turbulent nonpremixed combustion to the sub-grid flamelet model. ϵ is a well established parameter in turbulence theory (Jones & Launder, 1972; Pope, 2000) and will be used as tracking variable to determine the parameters (vorticity and strain rate) at the smallest scale of turbulence that are constraints for the flamelet model. Specifically, we work here with the rotational flamelet model presented by Sirignano (2022a), Sirignano (2022c), Hellwig *et al.* (2023a).

3 Basic Relations for Rotational Flamelet

Consider the transformation from the non-rotating coordinate system with space coordinates x, y, z and corresponding velocity components u, v, w to the system rotating about the z -axis through the origin with the coordinates ξ, χ, z and velocity components u_ξ, u_χ, z . The transformation displayed in Figure 1 is made from the Newtonian frame with rotating material (due to vorticity) to a rotating, non-Newtonian frame. Let the vorticity direction be the z direction in an orthogonal framework. Any x, y plane contains the directions of scalar gradients, major principal axis for compressive strain, and a principal axis for tensile strain. Note that the x, y, z directions are not correlated with coordinates on the resolved scale. ω is the vorticity magnitude on this sub-grid scale. x, y, z are transformed to ξ, χ, z wherein the material rotation is removed from the ξ, χ plane by having it rotate at angular velocity $d\theta/dt = \omega/2$ relative to x, y . Here, θ is the angle between

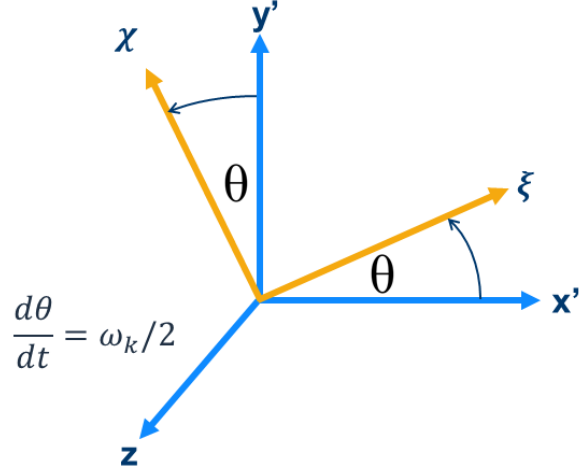


Figure 1: Transformation to ξ, χ, z' rotating coordinate system from x', y', z' Newtonian system. θ increases in the counterclockwise direction.

the x and ξ axes and simultaneously the angle between the y and χ axes. We take the sub-grid domain to be sufficiently small to consider a uniform value of ω across it.

The dependent and independent variables will be presented in dimensional form unless noted otherwise. The relations between the velocity components and spatial coordinates are given as

$$\xi = x \cos \theta + y \sin \theta ; \chi = y \cos \theta - x \sin \theta \quad (1)$$

$$u_\xi = u \cos \theta + v \sin \theta + \chi \frac{\omega}{2} ; u_\chi = v \cos \theta - u \sin \theta - \xi \frac{\omega}{2} \quad (2)$$

$$\frac{\partial u}{\partial x} = \frac{\partial u}{\partial \xi} \cos \theta - \frac{\partial u}{\partial \chi} \sin \theta ; \frac{\partial u}{\partial y} = \frac{\partial u}{\partial \xi} \sin \theta + \frac{\partial u}{\partial \chi} \cos \theta \quad (3)$$

$$\frac{\partial v}{\partial x} = \frac{\partial v}{\partial \xi} \cos \theta - \frac{\partial v}{\partial \chi} \sin \theta ; \frac{\partial v}{\partial y} = \frac{\partial v}{\partial \xi} \sin \theta + \frac{\partial v}{\partial \chi} \cos \theta \quad (4)$$

From Equation (1), it follows that $\sqrt{x^2 + y^2} = \sqrt{\xi^2 + \chi^2}$. Thus, the units of length are equal in both reference frames.

Differentiation of Equations (2), together with constraints that u_ξ is in-

dependent of χ and u_χ is independent of ξ , yields

$$\frac{\partial u_\xi}{\partial \xi} = \frac{\partial u}{\partial \xi} \cos\theta + \frac{\partial v}{\partial \xi} \sin\theta ; \quad \frac{\partial u_\xi}{\partial \chi} = 0 = \frac{\partial u}{\partial \chi} \cos\theta + \frac{\partial v}{\partial \chi} \sin\theta + \frac{\omega}{2} \quad (5)$$

$$\frac{\partial u_\chi}{\partial \xi} = \frac{\partial v}{\partial \xi} \cos\theta - \frac{\partial u}{\partial \xi} \sin\theta ; \quad \frac{\partial u_\chi}{\partial \chi} = 0 = \frac{\partial v}{\partial \chi} \cos\theta - \frac{\partial u}{\partial \chi} \sin\theta - \frac{\omega}{2} \quad (6)$$

From Equations (3) and (4), multiplications by $\cos\theta$ or $\sin\theta$, addition of equations, and use of $\cos^2\theta + \sin^2\theta = 1$ yields

$$\frac{\partial u_\xi}{\partial \xi} \cos\theta = \frac{\partial u}{\partial \xi} + \frac{\omega \sin\theta}{2} ; \quad \frac{\partial u_\chi}{\partial \chi} \cos\theta = \frac{\partial v}{\partial \chi} + \frac{\omega \sin\theta}{2} \quad (7)$$

Solution of four linear algebraic equations given by Equations (3) and (4) yields

$$\begin{aligned} \frac{\partial u}{\partial \xi} &= \frac{\partial u}{\partial x} \cos\theta + \frac{\partial u}{\partial y} \sin\theta ; & \frac{\partial u}{\partial \chi} &= \frac{\partial u}{\partial y} \cos\theta - \frac{\partial u}{\partial x} \sin\theta ; \\ \frac{\partial v}{\partial \xi} &= \frac{\partial v}{\partial x} \cos\theta + \frac{\partial v}{\partial y} \sin\theta ; & \frac{\partial v}{\partial \chi} &= \frac{\partial v}{\partial y} \cos\theta - \frac{\partial v}{\partial x} \sin\theta \end{aligned} \quad (8)$$

Use of Equations (8) to substitute into Equation (2) followed by division with $\cos\theta$ yields

$$\begin{aligned} \frac{\partial u_\xi}{\partial \xi} &= \frac{\partial u}{\partial x} + \left(\frac{\partial u}{\partial y} + \frac{\omega}{2} \right) \tan\theta \\ \frac{\partial u_\chi}{\partial \chi} &= \frac{\partial v}{\partial y} - \left(\frac{\partial v}{\partial x} - \frac{\omega}{2} \right) \tan\theta \end{aligned} \quad (9)$$

The inflow should be independent of θ position. That occurs if $\partial v/\partial x = -\partial u/\partial y = \omega/2$. This implies that the shear strain rate $S_{xy} = [\partial u/\partial y + \partial v/\partial x]/2 = 0$. Since w depends only on z and u and v are independent of z for the inflow, $S_{xz} = 0, S_{yz} = 0$ as well. Thereby, only normal strain rate occurs in the inflow for either coordinate system.

With the aim towards establishing scaling relations, the flamelet-related material in the following several sections is applied to incoming counterflow at some distance from the reaction zone. There, density, other scalar properties, strain rates can be considered as uniform; velocity gradients and scalar gradients will differ from values at the filtered scales of the resolved flow. Our scaling from resolved-scale values for RANS or LES will impose boundary conditions on the flamelet but will not prescribe directly the values in or near the reaction zone; in this critical manner, the approach differs from the Flamelet Progress Variable method.

4 Divergence and Curl of Velocity

Given the relation for the vorticity in the original reference frame,

$$\frac{\partial v}{\partial x} - \frac{\partial u}{\partial y} = \omega \quad (10)$$

and the relations in Equation (9), it follows that the divergence of velocity remains the same in both frames. Namely,

$$\frac{\partial u_\chi}{\partial \chi} + \frac{\partial u_\xi}{\partial \xi} + \frac{\partial w}{\partial z} = \frac{\partial u}{\partial x} + \frac{\partial v}{\partial y} + \frac{\partial w}{\partial z} \quad (11)$$

Identical dilatation will be felt in both coordinate frames.

For flow into the flamelet counterflow, u_ξ is only a function of ξ and u_χ is only dependent on χ , and the velocity derivatives $\partial u_\xi/\partial \chi$ and $\partial u_\chi/\partial \xi$ are each zero. Thereby, the curl of the velocity for the inflow in the rotating frame is zero.

$$\frac{\partial u_\chi}{\partial \xi} - \frac{\partial u_\xi}{\partial \chi} = 0 \quad (12)$$

That is, the vorticity does not appear explicitly for the inflow in the description within the rotating frame. It can have the important implicit effect through the centrifugal acceleration. In the flamelet interior core with varying density, velocity derivatives indicating shear strain and vorticity can develop because $u_\xi(\xi, \chi)$ and $w(\chi, z)$ can appear. However, since u_ξ is antisymmetric in ξ and w is antisymmetric in z , the circulations for the regions with total vorticity in the ξ - or χ -directions or added vorticity in the z -direction will each be zero.

5 Viscous Dissipation and Enstrophy

Consider first a general viscous flow configuration. Later, we will specifically address our flamelet-related configuration. The vorticity vector is the curl of the velocity, which written in tensor is $\omega_k = \epsilon_{ijk} \partial u_j / \partial x_i$ where ϵ_{ijk} is the Levi-Civita symbol. The enstrophy is defined as the dot product of the

vorticity vector with itself: $\vec{\omega} \cdot \vec{\omega} = \omega^2$. Thus, in the original coordinates,

$$\vec{\omega} = \left(\frac{\partial w}{\partial y} - \frac{\partial v}{\partial z}, \frac{\partial u}{\partial z} - \frac{\partial w}{\partial x}, \frac{\partial v}{\partial x} - \frac{\partial u}{\partial y} \right); \quad \vec{\omega} \cdot \vec{\omega} = \omega^2 \quad (13)$$

$$\begin{aligned} \omega^2 &= \left(\frac{\partial u}{\partial y} \right)^2 + \left(\frac{\partial u}{\partial z} \right)^2 + \left(\frac{\partial v}{\partial x} \right)^2 + \left(\frac{\partial v}{\partial z} \right)^2 + \left(\frac{\partial w}{\partial x} \right)^2 + \left(\frac{\partial w}{\partial y} \right)^2 \\ &\quad - 2 \left(\frac{\partial v}{\partial x} \frac{\partial u}{\partial y} + \frac{\partial u}{\partial z} \frac{\partial w}{\partial x} + \frac{\partial v}{\partial z} \frac{\partial w}{\partial y} \right) \end{aligned} \quad (14)$$

For a Newtonian fluid with dynamic coefficient of viscosity μ , application of Stokes hypothesis, and use of tensor notation, the viscous stress τ_{ij} and the viscous dissipation rate Φ are given as follows.

$$\tau_{ij} = \mu \left(\frac{\partial u_i}{\partial x_j} + \frac{\partial u_j}{\partial x_i} - \frac{2}{3} \delta_{ij} \frac{\partial u_k}{\partial x_k} \right) \quad (15)$$

$$\Phi = \tau_{ij} \frac{\partial u_i}{\partial x_j} = \mu \left(\frac{\partial u_i}{\partial x_j} \frac{\partial u_i}{\partial x_j} + \frac{\partial u_j}{\partial x_i} \frac{\partial u_i}{\partial x_j} - \frac{2}{3} \left[\frac{\partial u_k}{\partial x_k} \right]^2 \right) \quad (16)$$

$$\begin{aligned} \frac{\Phi}{\mu} &= \frac{4}{3} \left[\left(\frac{\partial u}{\partial x} \right)^2 + \left(\frac{\partial v}{\partial y} \right)^2 + \left(\frac{\partial w}{\partial z} \right)^2 \right] + \left(\frac{\partial u}{\partial y} \right)^2 + \left(\frac{\partial v}{\partial x} \right)^2 + 2 \frac{\partial u}{\partial y} \frac{\partial v}{\partial x} \\ &\quad - \frac{4}{3} \left[\frac{\partial u}{\partial x} \frac{\partial v}{\partial y} + \frac{\partial u}{\partial x} \frac{\partial w}{\partial z} + \frac{\partial v}{\partial y} \frac{\partial w}{\partial z} \right] \\ &\quad + \left[\left(\frac{\partial u}{\partial z} \right)^2 + \left(\frac{\partial v}{\partial z} \right)^2 + \left(\frac{\partial w}{\partial x} \right)^2 + \left(\frac{\partial w}{\partial y} \right)^2 + 2 \frac{\partial u}{\partial z} \frac{\partial w}{\partial x} + 2 \frac{\partial v}{\partial z} \frac{\partial w}{\partial y} \right] \end{aligned} \quad (17)$$

In our special flamelet case where u and v are independent of z , four terms on the last line of Equation (17) become zero-valued. The other two terms on that line are zero for the incoming flow where w depends only on z .

Consider now that $\omega/2 = \partial v/\partial x = -\partial u/\partial y$. Then, Equation (9) yields $\partial u/\partial x = \partial u_\xi/\partial \xi$ and $\partial v/\partial y = \partial u_\chi/\partial \chi$. Also, the last three terms on the first line of Equation (17) become $\omega^2/4 + \omega^2/4 - 2\omega^2/4 = 0$. Now, for the inflow, the viscous dissipation can be described by

$$\begin{aligned} \frac{\Phi}{\mu} &= \frac{4}{3} \left[\left(\frac{\partial u}{\partial x} \right)^2 + \left(\frac{\partial v}{\partial y} \right)^2 + \left(\frac{\partial w}{\partial z} \right)^2 - \frac{\partial u}{\partial x} \frac{\partial v}{\partial y} - \frac{\partial u}{\partial x} \frac{\partial w}{\partial z} - \frac{\partial v}{\partial y} \frac{\partial w}{\partial z} \right] \\ &= \frac{4}{3} \left[\left(\frac{\partial u_\xi}{\partial \xi} \right)^2 + \left(\frac{\partial u_\chi}{\partial \chi} \right)^2 + \left(\frac{\partial w}{\partial z} \right)^2 - \frac{\partial u_\xi}{\partial \xi} \frac{\partial u_\chi}{\partial \chi} - \frac{\partial u_\xi}{\partial \xi} \frac{\partial w}{\partial z} - \frac{\partial u_\chi}{\partial \chi} \frac{\partial w}{\partial z} \right] \end{aligned} \quad (18)$$

The last relation for Φ/μ is identical to the form to be found from direct application of Equation (17) using the velocity components and coordinates

for the rotating frame. Essentially, the wheel-like dissipation causes no strain or additional dissipation, yielding the same dissipation rates to be calculated for either frame.

If a portion or all of the flow is divergence free, the effect of bulk viscosity is absent and Equations (15,16,18) may be written as

$$\begin{aligned} \tau_{ij} &= \mu \left(\frac{\partial u_i}{\partial x_j} + \frac{\partial u_j}{\partial x_i} \right) ; \quad \Phi = \tau_{ij} \frac{\partial u_i}{\partial x_j} = \mu \left(\frac{\partial u_i}{\partial x_j} \frac{\partial u_i}{\partial x_j} + \frac{\partial u_j}{\partial x_i} \frac{\partial u_i}{\partial x_j} \right) ; \\ \frac{\Phi}{\mu} &= 2 \left[\left(\frac{\partial u}{\partial x} \right)^2 + \left(\frac{\partial v}{\partial y} \right)^2 + \left(\frac{\partial w}{\partial z} \right)^2 \right] = 2 \left[\left(\frac{\partial u_\xi}{\partial \xi} \right)^2 + \left(\frac{\partial u_\chi}{\partial \chi} \right)^2 + \left(\frac{\partial w}{\partial z} \right)^2 \right] \end{aligned} \quad (19)$$

If the divergence of the momentum equation is taken for the case of constant density and constant coefficient of viscosity, we obtain with use of relations for Φ and ω^2

$$\begin{aligned} \frac{1}{\rho} \frac{\partial^2 p}{\partial x_i^2} &= - \frac{\partial}{\partial x_i} \left(u_j \frac{\partial u_i}{\partial x_j} \right) + \mu \frac{\partial^2}{\partial x_j^2} \left(\frac{\partial u_i}{\partial x_i} \right) \\ &= - \frac{\partial u_j}{\partial x_i} \frac{\partial u_i}{\partial x_j} - u_j \frac{\partial}{\partial x_j} \frac{\partial u_i}{\partial x_i} + \mu \frac{\partial^2}{\partial x_j^2} \left(\frac{\partial u_i}{\partial x_i} \right) \\ &= - \frac{\partial u_j}{\partial x_i} \frac{\partial u_i}{\partial x_j} - 0 + 0 = - \frac{\partial u_i}{\partial x_j} \frac{\partial u_i}{\partial x_j} + \omega^2 = \frac{\omega^2}{2} - \frac{\Phi}{2\mu} \end{aligned} \quad (20)$$

Realize that, in the rotating frame the centrifugal acceleration is given as $\vec{a} = (\xi\omega^2/4, \chi\omega^2/4)$. Thereby, $\nabla \cdot \vec{a} = \omega^2/2$. Since viscous dissipation maintains the same value in both systems, the implication is that the Laplacian of the pressure is identical in both systems. In order to maintain a pressure maximum and thereby a stagnation point, the centrifugal effect must be overcome by the effect of the strain rate; i.e., $\omega^2 < A_{ij}A_{ij}$ where $A_{ij} \equiv \partial u_i / \partial x_j$. Note that Φ/μ is independent of the coefficient of viscosity. The balance here relates to strain rate and not viscous action. Actually, the viscous effect was removed by the divergence operation.

Here, we have a strong argument for the importance of the balance of vorticity magnitude and strain-rate magnitude or, more precisely, the balance between dissipation rate and enstrophy. There are many studies on these quantities, especially for incompressible flows (Johnson, 2021; Johnson & Wilczek, 2023; Yeung *et al.*, 2012). If enstrophy ω^2 becomes too large compared to the dissipation rate divided by dynamic viscosity Φ/μ , the pressure Laplacian becomes positive, thereby disallowing the flamelet counterflow

possibility since the required stagnation point located at a pressure maxima cannot occur. This vital issue of balance cannot be addressed in a formulation that neglects vorticity and only addresses strain rate. For incompressible turbulent flow, this balance has been addressed by Yeung *et al.* (2012) who find that the temporal statistics for both quantities present similar magnitudes. They find large values of each parameter tend to occur together with $\Phi/\mu > \omega^2$ for 60-65 percent of the data. Although the study does not include dilatation, it shows support for the concept of mixing and reaction occurring in rotating counterflows provided by the turbulent eddies. In cases where combustion has mixing as rate-controlling, the higher-strain-rate (and thereby smaller) eddies would provide the highest burning rates (provided the mixing rate does not exceed the reaction rate).

Φ gives the kinetic energy dissipation rate per unit volume. Division by density gives ϵ , the kinetic energy dissipation rate per unit mass, commonly used in turbulence modeling. We may write enstrophy as

$$\omega^2 = \frac{\partial u_i}{\partial x_j} \frac{\partial u_i}{\partial x_j} - 2 \frac{\partial u_i}{\partial x_j} \frac{\partial u_j}{\partial x_i} + \frac{\partial u_j}{\partial x_i} \frac{\partial u_j}{\partial x_i} = 2 \left[\frac{\partial u_i}{\partial x_j} \frac{\partial u_i}{\partial x_j} - \frac{\partial u_i}{\partial x_j} \frac{\partial u_j}{\partial x_i} \right] \quad (21)$$

Then, with account for bulk viscosity, Equations (16) and (21) yield

$$\epsilon = \frac{\Phi}{\rho} = \nu \left(2 \frac{\partial u_i}{\partial x_j} \frac{\partial u_i}{\partial x_j} - \frac{2}{3} \left[\frac{\partial u_k}{\partial x_k} \right]^2 - \frac{\omega^2}{2} \right) \quad (22)$$

where $\nu = \mu/\rho$ is the kinematic viscosity. For the constant-density inflow, we may write

$$\begin{aligned} \epsilon &= 2\nu \left[\left(\frac{\partial u_\xi}{\partial \xi} \right)^2 + \left(\frac{\partial u_\chi}{\partial \chi} \right)^2 + \left(\frac{\partial w}{\partial z} \right)^2 \right] = 2\nu [(S^* S_1)^2 + S^{*2} + (S^* S_2)^2] \\ &= 2\nu S^{*2} [S_1^2 + 1 + S_2^2] = 4\nu S^{*2} [S_1^2 + 1 - S_1] \end{aligned} \quad (23)$$

where the definition $S_1 + S_2 = 1$ has been entered. The implication of Equation (23) is that if ϵ were known from the resolved scale, a relation between S^* and S_1 is established for the rotational flamelet. This relation could be useful for the Flamelet Progress Variable model as well. For example, with $S_1 = 1/2$, we find $S^* = \sqrt{\epsilon/(3\nu)}$, its peak value. As S_1 varies in the range $0 \leq S_1 \leq 1$, S^* varies narrowly between $\sqrt{\epsilon/(4\nu)}$ and $\sqrt{\epsilon/(3\nu)}$. In the range $-1 \leq S_1 \leq 0$ (with inward swirl), S^* varies more strongly between $\sqrt{\epsilon/(12\nu)}$ and $\sqrt{\epsilon/(3\nu)}$.

Viscous dissipation actually occurs over a range of the smallest scales and not totally at the Kolmogorov scale. Therefore, we have reason to multiply ϵ in Equation (22) by the coefficient C_{vd} where $C_{vd} < 1$.

6 Kinetic Energy

With use of Equation (2), it can be readily found that

$$\left(u_\xi - \frac{\omega\chi}{2}\right)^2 + \left(u_\chi + \frac{\omega\xi}{2}\right)^2 + w^2 = u^2 + v^2 + w^2 \quad (24)$$

Specifically, if account is taken of the moving ξ, χ coordinates, we see that the same kinetic energy is implied for both frames of reference; although, explicit appearance of the rotational portion of that energy is not given in the rotating frame.

For the incompressible counterflow structure, we can write

$$\begin{aligned} u_\xi &= \frac{\partial u_\xi}{\partial \xi} \xi ; \quad u_\chi = \frac{\partial u_\chi}{\partial \chi} \chi ; \quad w = \frac{\partial w}{\partial z} z \\ \frac{u^2 + v^2 + w^2}{2} &= \frac{1}{2} \left(\frac{\partial u_\xi}{\partial \xi}\right)^2 \xi^2 + \frac{1}{2} \left(\frac{\partial u_\chi}{\partial \chi}\right)^2 \chi^2 + \frac{1}{2} \left(\frac{\partial w}{\partial z}\right)^2 z^2 \\ &\quad + \frac{1}{8} \omega^2 (\xi^2 + \chi^2) + \left(\frac{\partial u_\chi}{\partial \chi} - \frac{\partial u_\xi}{\partial \xi}\right) \frac{\omega \xi \chi}{2} \end{aligned} \quad (25)$$

The right side of Equation (23) requires knowledge of three quantities for rotational flamelet theory: S^* , S_1 , and vorticity ω . The Kolmogorov scale can be used to estimate the lengths. The kinetic energy per unit mass here is based on Kolmogorov scale velocity fluctuations; so, the value will be less than the statistical value for turbulence kinetic energy k . If a relation between the two kinetic energies is provided, knowledge of k provides a relationship between those three quantities. Thereby, Equations (22) and (23) have potential to be used with knowledge of ϵ from resolved-scale computation to determine the needed inflow parameters S^* and ω for the rotational flamelet model.

The turbulence kinetic energy cascade is classically described by assuming the rate of turbulence kinetic energy transfer from any scale to a lower scale is identical. That means $\epsilon \approx (u')^2/\tau' \approx (u')^3/l'$, where u' , τ' and l' are the associated velocity, time, and length scales for a given portion of the

turbulence spectrum. At the Kolmogorov scale (i.e., the smallest scales), those scales are u_κ , τ_κ , and κ , respectively. At that Kolmogorov scale, the Reynolds number $Re = u_\kappa \kappa / \nu \approx 1$ and the strain rate $u_\kappa / \kappa \approx \epsilon / u_\kappa^2$ is the largest value across all scales.

We will use the relations from Pope, Page 185 (Pope, 2000); the Kolmogorov velocity $u_\kappa \approx (\epsilon \nu)^{1/4}$ and the Kolmogorov length $\kappa \approx (\nu^3 / \epsilon)^{1/4}$. We will average kinetic energy over a volume equal to κ^3 . The last term in Equation (23) shows antisymmetry, taking positive values in two quadrants and negative values of identical magnitudes in the other two quadrants of any ξ, χ plane. Thereby, they have no consequence for our averaging. Equation (23) now yields after averaging the right side and relating the left side to ϵ ,

$$\begin{aligned} C_{ke}(\epsilon \nu)^{1/2} &= S^{*2} \frac{\nu^{3/2}}{\epsilon^{1/2}} \left[S_1^2 + 1 + S_2^2 + 2 \left(\frac{\omega}{2S^*} \right)^2 \right] \\ C_{ke} \frac{\epsilon}{\nu} &= 2S^{*2} \left[S_1^2 + 1 - S_1 + \left(\frac{\omega}{2S^*} \right)^2 \right] \end{aligned} \quad (26)$$

C_{ke} is a nondimensional coefficient of $O(1)$ that appears in the averaging process for the kinetic energy term on the left side of Equations (23). It accounts for both approximations made in averaging and adjusted decrease in kinetic energy at the Kolmogorov scale because dissipation has occurred over a range of the smallest scales.

7 Scaling of Velocity Gradients

Now, we have a relation where, given the value of ϵ / ν and a statistical estimate for S_1 , we can relate S^* to ω . Together with Equation (21), we have two independent relations for determining S^* and ω for the rotational flamelet given the resolved scale RANS solutions. Combination of Equations (21) and (24) yields a more direct equation for determining ω .

$$\frac{\omega^2}{2} = \left(C_{ke} - \frac{1}{2} C_{vd} \right) \frac{\epsilon}{\nu} \quad (27)$$

Interestingly, it is a quadratic equation that yields two solutions for ω of equal magnitude and opposite direction; the direction of rotation is irrelevant for major issues. The magnitudes of S_1 and S_2 are also irrelevant to the magnitude of ω . The vorticity is of the same order of magnitude as the applied compressive strain rate. The value of the enstrophy (i.e., ω^2) will

determine whether the pressure Laplacian from Equation (19) is negative, which is needed to allow the counterflow flamelet to exist. Specifically,

$$\frac{1}{\rho} \frac{\partial^2 p}{\partial x_i^2} = \frac{\omega^2}{2} - \frac{\Phi}{2\mu} = \left(C_{ke} - \frac{1}{2}C_{vd}\right) \frac{\epsilon}{\nu} - C_{vd} \frac{\epsilon}{2\nu} = \left(C_{ke} - C_{vd}\right) \frac{\epsilon}{\nu} \quad (28)$$

The positive coefficient needs a value $C_{ke} < C_{vd}$ in order for the counterflow to exist. A given value of ϵ will produce one acceptable ω value and one acceptable S^* value. Thereby, we expect one acceptable SDR_{max} value. However, that value cannot be captured by knowing S^* alone.

It is found that ϵ is the meaningful tracking variable. From the knowledge of ϵ and fluid properties, with a choice for the parameter S_1 , the values of S^* , dimensional ω , the pressure Laplacian, and the viscous dissipation follow. Specifically,

$$\begin{aligned} S^* &= \frac{1}{2} \sqrt{\frac{C_{vd} \epsilon}{\nu[S_1^2 + 1 - S_1]}} \quad ; \quad \omega = \sqrt{\frac{2[C_{ke} - C_{vd}/2] \epsilon}{\nu}} \quad ; \\ \frac{1}{\rho} \frac{\partial^2 p}{\partial x_i^2} &= \left(C_{ke} - C_{vd}\right) \frac{\epsilon}{\nu} \quad ; \quad \frac{\Phi}{\mu} = C_{vd} \frac{\epsilon}{\nu} \end{aligned} \quad (29)$$

We must be sure that, with any application of the flamelet model for Kolmogorov or near-Kolmogorov scales, $(1/2)C_{ke} < (3/4)C_{vd}$ is at least supportable in a statistical sense. No counterflow-based flamelet model can be justified with a positive pressure Laplacian.

Using the resolved-scale non-dimensionalization scheme discussed in Appendix B, it can be shown that

$$\begin{aligned} \frac{S^*}{\beta_\infty} &= \frac{1}{2\beta_\infty} \left(\frac{C_{vd} \epsilon}{\nu[S_1^2 + 1 - S_1]} \right)^{1/2} = \frac{1}{2} \left(\frac{C_{vd} Re \epsilon_{nd}}{S_1^2 + 1 - S_1} \right)^{1/2} \quad ; \\ \frac{\omega^2}{2S^{*2}} &= \frac{[C_{ke} - C_{vd}/2] \epsilon}{\nu S^{*2}} = 2 \frac{[2C_{ke} - C_{vd}][S_1^2 + 1 - S_1]}{C_{vd}} \end{aligned} \quad (30)$$

Plots of the flammability curve for the rotational flamelet, with curves of nondimensional T_{max} , SDR_{max} , or integrated burning rate versus $\sqrt{\epsilon/\nu_\infty}$, are informative, e.g., plots of the Hellwig *et al.* (2023a) flamelet results (integrated burning rate, T_{max} , and SDR_{max}) versus ϵ at a fixed S_1 .

ϵ should not be considered a ‘‘progress variable’’ since its value can increase or decrease in any spacial direction or in time. We should think in terms of a ‘‘tracking variable’’ rather than a progress variable.

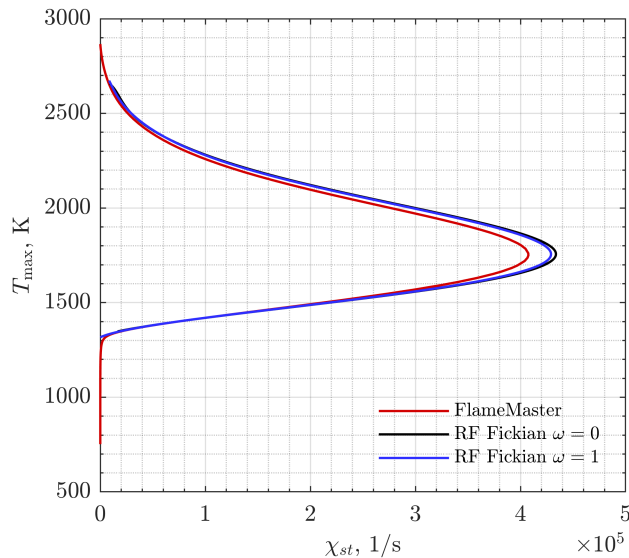


Figure 2: Comparison of three flamelet models for $\text{H}_2/\text{N}_2 - \text{O}_2$ diffusion flames with T_{max} as a function of stoichiometric SDR value (χ_{st}): red, Progress Variable result from FlameMaster; black, Rotational Flamelet with Fickian diffusion at $\text{Le}=1$ and zero vorticity; blue, Rotational Flamelet with Fickian diffusion at $\text{Le}=1$ and vorticity.

8 Flamelet Connection with ϵ

In this section, results from five flamelet models for $\text{H}_2/\text{N}_2 - \text{O}_2$ combustion are presented. These models are generated for an oxidizer stream consisting of pure O_2 and a fuel stream consisting of an equimolar mixture of H_2 and N_2 . Both streams enter at 300 K, with a background pressure of 10 atm. Gas-phase kinetics, thermal properties, and transport properties are calculated using a nine-species reduction of Version 1.0 of the Foundational Fuel Chemistry Model reaction mechanism (FFCM-1) developed and tested in Smith *et al.* (2016); Tao *et al.* (2018). Nitrogen is treated as an inert species.

The first set of results pertains to the classical flamelet model, where key quantities of interest—such as temperature, species mass fractions, and heat release—are determined by solving the classical flamelet equations in mixture fraction space (Peters (1984, 2000); Pierce & Moin (2004)). In this context, the mixture fraction is denoted by Z . Unlike the Rotational Flamelet model, the momentum equation is not explicitly solved in the clas-

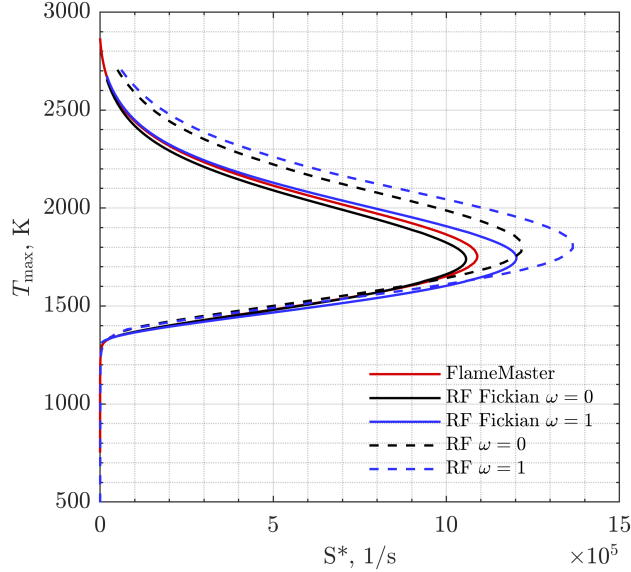


Figure 3: Comparison of five flamelet models for $\text{H}_2/\text{N}_2 - \text{O}_2$ diffusion flames with T_{max} as a function of applied compressive strain rate S^* : red, Progress Variable result from FlameMaster; black, Rotational Flamelet with Fickian diffusion at $\text{Le}=1$ and zero vorticity; blue, Rotational Flamelet with Fickian diffusion at $\text{Le}=1$ and vorticity; dashed black, Rotational Flamelet with preferential diffusion and zero vorticity; dashed blue, Rotational Flamelet with preferential diffusion and vorticity.

sical flamelet model. Instead, its effects are introduced through an assumed form of the scalar dissipation rate, specifically $\chi(Z) = \frac{2S^*}{\pi} \exp(2\text{erfc}^{-1}(2Z)^2)$ as specified in Peters (2000). Note that by not explicitly solving the momentum equation, this formulation does not address the effects of vorticity on the flame. The results for the classical flamelet model are obtained using the FlameMaster code developed by Pitsch (2022).

The remaining four sets of results correspond to Rotational Flamelet models. These include Rotational Flamelet models with and without vorticity using Fickian diffusion at unity Lewis number, as well as models with and without vorticity using preferential mass diffusion. These rotational flamelet models were generated using an in-house MATLAB code developed in Hellwig *et al.* (2023a,b). To ensure optimal comparability between the classical and Rotational Flamelet models, equal transverse strain rates ($S_1 = S_2$) are employed in the rotational model computations. That is, S_1 is set to $1/2$

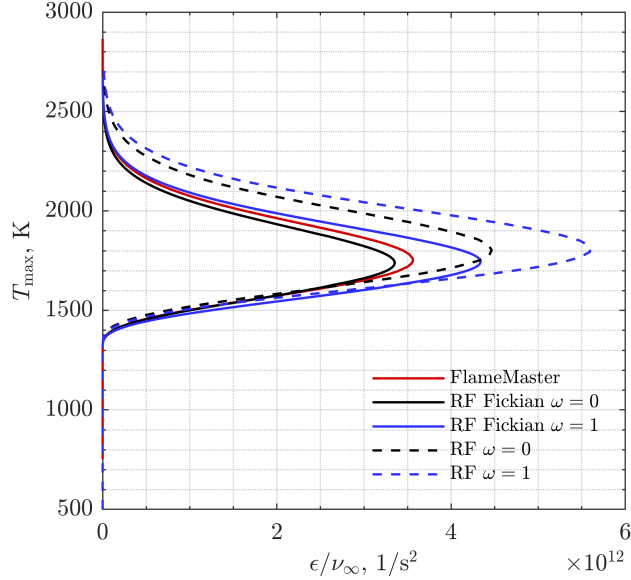


Figure 4: Comparison of five flamelet models for $\text{H}_2/\text{N}_2 - \text{O}_2$ diffusion flames with T_{max} as a function of ϵ/ν_∞ : red, classical result from FlameMaster; black, Rotational Flamelet with Fickian diffusion at $Le=1$ and zero vorticity; blue, Rotational Flamelet with Fickian diffusion at $Le=1$ and vorticity; dashed black, Rotational Flamelet with preferential diffusion and zero vorticity; dashed blue, Rotational Flamelet with preferential diffusion and vorticity.

in the equations presented above. This value provides the closest approximation to the classical model’s two-dimensional axisymmetric counterflow configuration.

The results focus on three main parameters: maximum flamelet temperature, integrated burning rate, and stoichiometric flamelet scalar dissipation rate. These parameters are examined as functions of both inflow strain rate S^* and ϵ . The latter serves to highlight the connection between the flamelet and the resolved scale. Note that in the previous sections, unlike some other works, ω is dimensional with identical units as S^* . However, in this section, ω is non-dimensionalized by S^* , following the approaches used by Sirignano (2022*c,a,b*) and Hellwig *et al.* (2023*a,b*).

Figure 2 presents the maximum flamelet temperature as a function of the stoichiometric scalar dissipation rate, commonly known as S-shaped curves. This figure serves as a common reference for readers familiar with flamelet

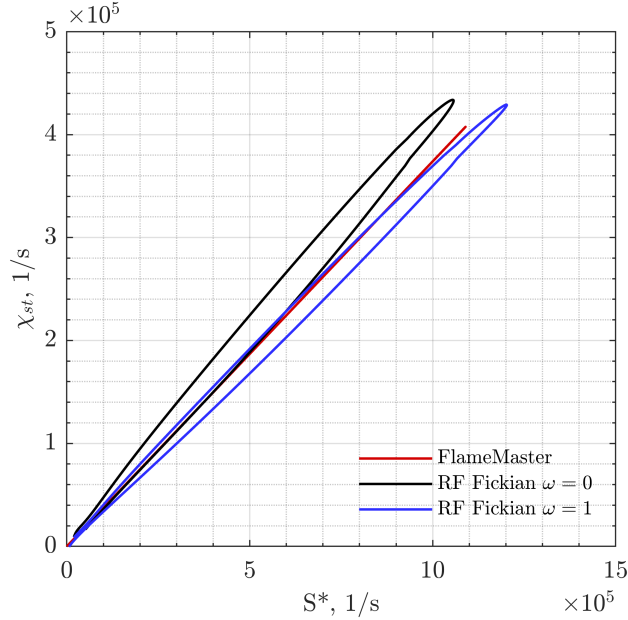


Figure 5: Comparison of three flamelet models for $\text{H}_2/\text{N}_2 - \text{O}_2$ diffusion flames with χ_{st} as a function of S^* : red, classical result from FlameMaster; blue, Rotational Flamelet with Fickian diffusion at $\text{Le}=1$ and zero vorticity; black, Rotational Flamelet with Fickian diffusion at $\text{Le}=1$ and vorticity.

modeling based on the classical mixture fraction formulation. Only three curves are shown, as the scalar dissipation rate is not applicable in cases of preferential diffusion. Differences between the classical and rotational models are evident and anticipated, reflecting the variations in their formulations. The rotational models demonstrate marginally extended flammability limits for both vorticity values. While this presentation, which parametrizes the flame state using scalar dissipation rate, may suggest that vorticity has a negligible impact, it will be shown later that relying on χ to describe the flame state is misleading and obscures the significant implications of accounting for vorticity.

Figure 3 displays the same S-shaped curves, but now parameterized by the inflow strain rate S^* . For the classical model, the S-shaped curve plotted against strain rate remains qualitatively similar to that in Figure 2. This is because S^* is related to χ_{st} by a constant through assumed functional form of $\chi(Z)$. However, in the case of the rotational models—where $\chi(Z)$ is not

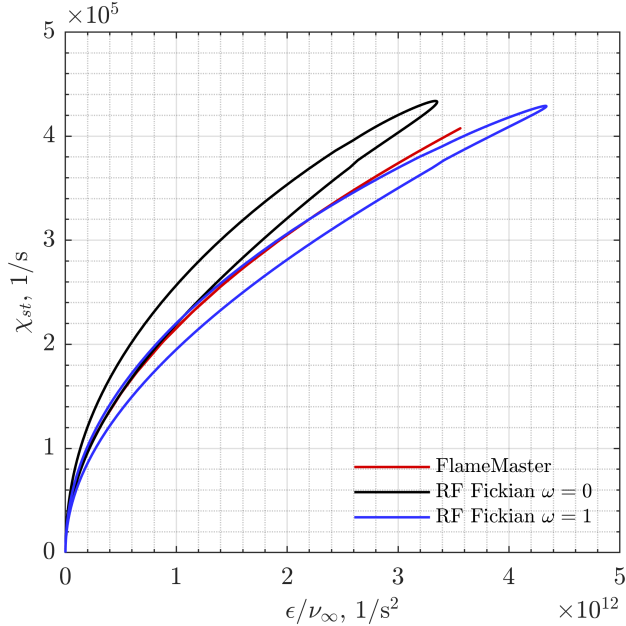


Figure 6: Comparison of three flamelet models for $\text{H}_2/\text{N}_2 - \text{O}_2$ diffusion flames with χ_{st} as a function of ϵ/ν_∞ : red, classical result from FlameMaster; black, Rotational Flamelet with Fickian diffusion at $\text{Le}=1$ and zero vorticity; blue, Rotational Flamelet with Fickian diffusion at $\text{Le}=1$ and vorticity.

assumed but instead determined by solving the momentum equation—the effect of vorticity on the flamelet becomes more pronounced. The zero-vorticity case closely resembles the classical flamelet model, which is expected, as the absence of vorticity aligns with the classical formulation where vorticity is not considered. However, when vorticity is included, a significant increase in the extinction inflow strain rate is observed.

Additionally, two more curves are plotted for Rotational Flamelet models with preferential diffusion, corresponding to dimensionless vorticity values of zero and one. Once again, the presence of vorticity extends the flammability limit. Moreover, the use of preferential diffusion results in distinct differences, including increased maximum temperature and broader flammability limits compared to the Fickian diffusion models.

In Figure 4, the maximum temperature is parameterized by ϵ/ν_∞ . To achieve this, S^* is related to ϵ/ν using the first expression from Equation 29. Although the value of C_{vd} is not known at this time, a value of 1 has been

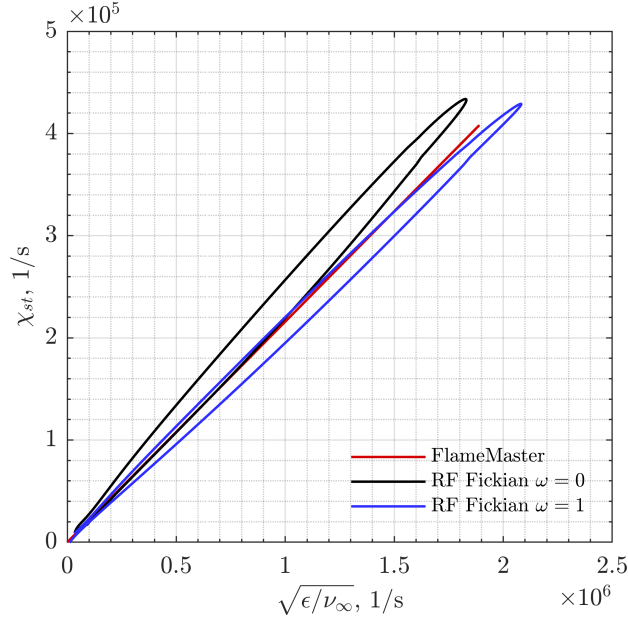


Figure 7: Comparison of three flamelet models for $\text{H}_2/\text{N}_2 - \text{O}_2$ diffusion flames with χ_{st} as a function of $\sqrt{\epsilon/\nu_\infty}$: red, classical result from FlameMaster; black, Rotational Flamelet with Fickian diffusion at $\text{Le}=1$ and zero vorticity; blue, Rotational Flamelet with Fickian diffusion at $\text{Le}=1$ and vorticity.

selected for demonstration purposes. With $S_1=1/2$, the inflow strain rate becomes $S^* = \sqrt{\epsilon/(3\nu)}$. This illustrates how ϵ , which is determined from the resolved scale, can serve as a tracking effectively connecting the flamelet to resolved scale computations.

Walsh *et al.* (2024) employed a Flamelet Progress Variable (FPV) approach coupled with the RANS equations to study methane-vitiated air combustion in highly accelerating mixing layers. In the FPV approach, χ_{st} is monotonically mapped to a progress variable that is defined at the sub-scale but tracked at the resolved scale using a constructed transport equation. However, as shown in Figure 4, it is conceivable to replace the progress variable with ϵ , which is directly available from the resolved-scale RANS equations.

Figures 5 and 6 plot stoichiometric scalar dissipation rates χ_{st} for the three Fickian models against S^* and ϵ/ν_∞ , respectively. While χ_{st} has been chosen for consistency with the classical models, there is no inherent reason

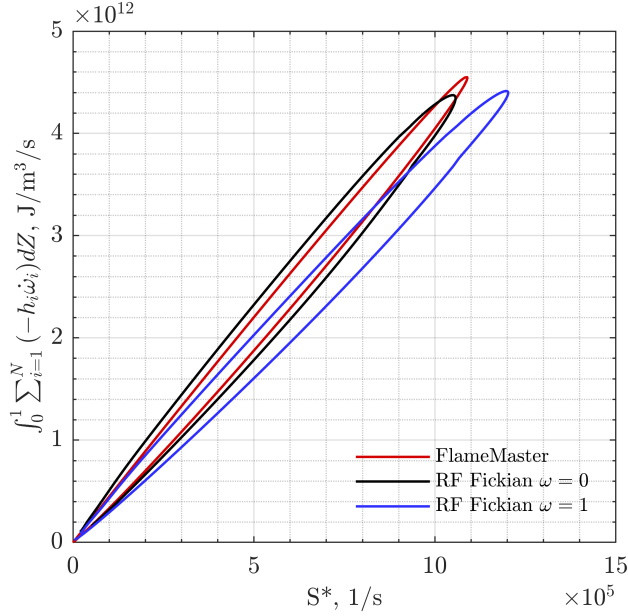


Figure 8: Comparison of three flamelet models for $\text{H}_2/\text{N}_2 - \text{O}_2$ diffusion flames with integrated burning rate as a function of S^* : red, classical result from FlameMaster; black, Rotational Flamelet with Fickian diffusion at $\text{Le}=1$ and zero vorticity; blue, Rotational Flamelet with Fickian diffusion at $\text{Le}=1$ and vorticity.

why χ_{max} could not be used instead. The χ_{st} used in the classical model, represented by the red line, is bijective and grows linearly with S^* , as a result of the assumed functional form of $\chi(Z, \omega)$. As previously discussed, in the Rotational Flamelet model, scalar dissipation is not assumed but determined by solving the momentum equation. The differences between the blue and black curves clearly demonstrate how scalar dissipation rate becomes a function of vorticity, i.e., $\chi(Z, \omega)$. Furthermore, contrary to the classical model, stable and unstable solutions have distinct χ_{st} values.

This dependence of χ on ω has significant implications. When viewing these figures alongside Figure 2, it becomes evident that for a given value of ϵ determined from the resolved scale, which imposes a corresponding S^* value, different vorticity values result in two distinct χ_{st} values, leading to two different flamelet solutions along the S-shaped curve. These solutions exhibit different maximum temperatures and integrated burning rates, regardless of

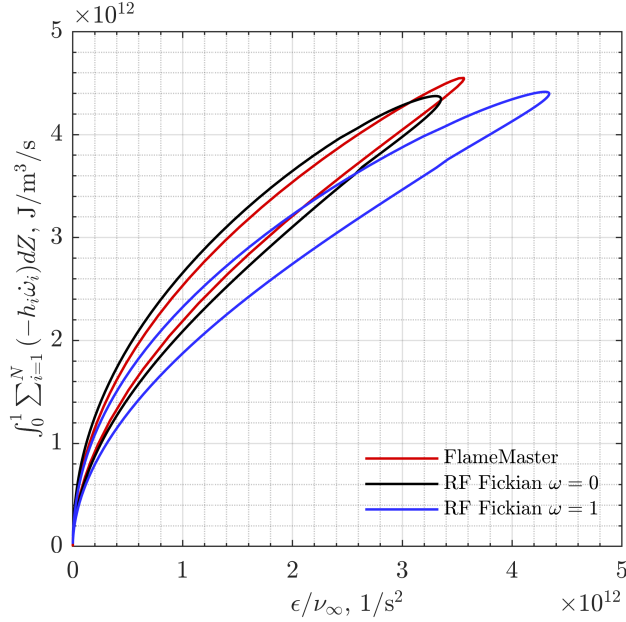


Figure 9: Comparison of three flamelet models for $\text{H}_2/\text{N}_2 - \text{O}_2$ diffusion flames with integrated burning rate as a function of ϵ/ν_∞ : red, classical result from FlameMaster; black, Rotational Flamelet with Fickian diffusion at $\text{Le}=1$ and zero vorticity; blue, Rotational Flamelet with Fickian diffusion at $\text{Le}=1$ and vorticity.

the fact that the S-shaped curves for different vorticity values collapse onto each other when parameterized by χ_{st} . This clearly shows that a flamelet solution cannot be determined based on S^* alone.

Figure 7 shows the same χ_{st} curves plotted against the square root of ϵ/ν_∞ . ϵ is the rate of dissipation of k , the turbulence kinetic energy per unit mass. It follows that the magnitude of velocity fluctuation decays at a rate proportional to $\sqrt{\epsilon}$. If we assume that a scalar fluctuation decreases proportionately to velocity and χ represents a rate of dissipation for a scalar fluctuation, the proportionality of χ and $\sqrt{\epsilon}$ are observed and expected.

More relevant than flame temperature is the heat release, which will in practice be the parameter extracted from the flamelet model and introduced into the resolved-scale computations. Figures 8 and 9 depict the integrated burning rate for the three Fickian models as functions of S^* and ϵ/ν_∞ , respectively. Here, the integrated burning rate is calculated as the heat release

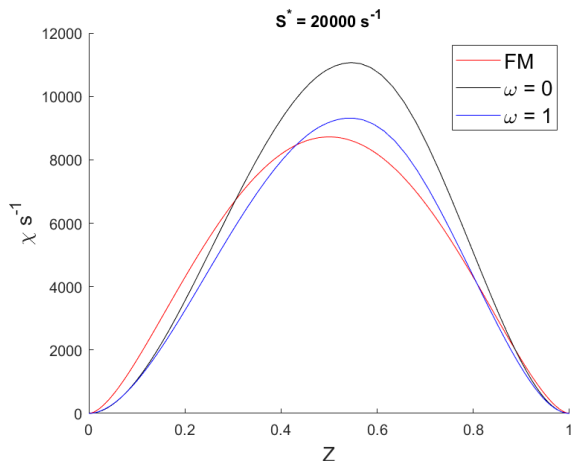


Figure 10: Comparison of three flamelet models for $\text{H}_2/\text{N}_2 - \text{O}_2$ diffusion flames with SDR as a function of mixture fraction Z : red, classical from FlameMaster; black, Rotational Flamelet with Fickian diffusion at $Le=1$ and zero vorticity; blue, Rotational Flamelet with Fickian diffusion at $Le=1$ and vorticity.

rate integrated over Z . All three models show that the integrated burning rate increases in a nearly linear manner with S^* , indicating that it grows as the scale decreases. As expected, the Rotational Flamelet model with zero vorticity most closely resembles the classical model, with differences in integrated burning rates due to distinctions in the underlying formulations of the two models. In the presence of vorticity (blue curve), the integrated burning rate shows a significant decrease compared to the zero-vorticity case.

Hellwig *et al.* (2023b) observed similar behaviour for integrated burning rate of H_2O plotted against S^* , showing a decrease in burning rates with increasing vorticity magnitude. Additionally, they found that when this parameter is plotted against χ_{st} , all cases with different vorticity magnitude collapse onto a single curve. However, as was show in Figures 2 and 5, it is the combination of knowledge of both S^* and ω (or simply ϵ) that determines an appropriate value of χ_{st} , leading to different points along these collapsed curves.

Figures 10 and 11 are examples of scalar dissipation rate χ , versus mixture fraction Z , for $\text{H}_2, \text{O}_2, \text{N}_2$ combustion and JP-5, air combustion, respectively. The blue and black curves illustrate the difference in scalar dissipation rate

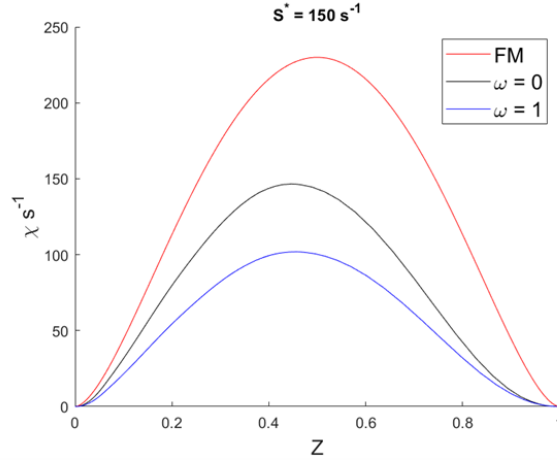


Figure 11: Comparison of three flamelet models for *JP5*-Air diffusion flames with *SDR* as a function of mixture fraction Z : red, classical result from FlameMaster; black, Rotational Flamelet with Fickian diffusion at $Le=1$ and zero vorticity; blue, Rotational Flamelet with Fickian diffusion at $Le=1$ and vorticity.

created by solving the momentum equations with vorticity in addition to the energy and species continuity equations. Clearly, vorticity has an effect on scalar dissipation rate and will thus alter the solution of the flamelet equations.

Furthermore, the peak of the scalar dissipation rate curve shows bias towards the stream with higher thermal diffusivity. This is seen from the H_2, O_2, N_2 peak sloping toward the fuel stream while the JP-5 peaks slopes away from the fuel stream. For $Le=1$, the mass diffusivity value is set to the thermal diffusivity value which is the product of density and specific heat in the denominator. Both terms in that denominator product minimize on the fuel-rich (fuel-lean) side for $H_2/N_2 - O_2$ (JP5-Air), causing diffusivity to maximize on that side. This results in dZ/dy , its square, and the coefficient D maximizing and causing χ to maximize on that preferred side. Let us, for the sake only of argument and display here, consider that, in the vicinity of maximum SDR, the velocity $v = -S^*y$ and D is approximately constant over a neighborhood. Treatment of the second-order ODE for $Z(y)$ as a first-order ODE for dZ/dy yields a local behavior where $dZ/dy \propto \exp[-S^*y^2/(2D)]$ and $\chi \propto D \exp[-S^*y^2/D]$. The larger D in the denominator of the exponent

causes a slower decline from the maximum value and thereby a larger value of the exponential term as well as its coefficient. This difference in thermal diffusivity for unitary Lewis number is due to the relatively high specific heat for JP-5 and O₂ relative to their respective opposing streams.

Since the scalar dissipation rate is proportional to strain rate, we should expect $SDR_{max}/S^* \propto \epsilon^{1/2}$ and scalar gradients should behave as $\epsilon^{1/4}$.

There are remaining questions. Each pair of values for vorticity and strain rate (at the same value for ϵ/ν) produce both a stable and an unstable branch. The appearance of the stability issue is not a mechanical impact but rather a thermal impact that relates to balance between chemical energy conversion rate on one hand and heat transfer rate on the other hand.

Statistical data on the values of S_1 and S_2 for reacting flows would be very useful. It likely would come from DNS, but experiments might be useful.

A key conclusion here is that a flamelet model that did not consider vorticity would be unable to match key physical parameters determined on the resolved scale.

References

- ASHURST, W. T., KERSTEIN, A. R., KERR, R. M. & GIBSON, C. H. 1987 Alignment of vorticity and scalar gradient with strain rate in simulated navier-stokes turbulence. *Physics of Fluids* **30**, 2343–52.
- BATCHELOR, G. K. 1967 *An Introduction to Fluid Dynamics*. Cambridge, UK: Cambridge University Press.
- BILGER, R. W. 1976 The structure of diffusion flames. *Combustion Science and Technology* **13**, 155–70.
- BORATAV, O. N., ELGHOBASHI, S. E. & ZHONG, R. 1996 On the alignment of the a-strain and vorticity in turbulent nonpremixed flames. *Physics of Fluids* **8**, 2251–53.
- BORATAV, O. N., ELGHOBASHI, S. E. & ZHONG, R. 1998 On the alignment of strain, vorticity and scalar gradient in turbulent, buoyant, non-premixed flames. *Physics of Fluids* **10**, 2260–67.
- BURGERS, J. M. 1948 A mathematical model illustrating the theory of turbulence. *Advances in Applied Mechanics* **1**, 171–199.

- BURGERS, J. M. 1951 Unpublished lectures on turbulence. *California Institute of Technology* **1**, 171–199.
- CETEGEN, B. M. & SIRIGNANO, W. A. 1988 Study of molecular mixing and a finite rate chemical reaction in a mixing layer. In *Proceedings of Twenty-Second Symposium (International) on Combustion*, pp. 489–94. Combustion Institute, Pittsburgh.
- CETEGEN, B. M. & SIRIGNANO, W. A. 1990 Study of mixing and reaction in the field of a vortex. *Combustion Science and Technology* **72**, 157–81.
- DRISCOLL, J. F., CHEN, J.H., SKIBA, A.W., CARTER, C.D., HAWKES, E. R. & WANG, H. 2020 Premixed flames subjected to extreme turbulence: Some questions and recent answers. *Prog. Energy Combust. Sci.* **76**, 100802.
- ELGHOBASHI, S. E. 1977 Studies in the predictions of turbulent diffusion flames. in *Studies in Convection: Theory, Measurement and Applications*, Editor B. E. Launder **2**, 141–189.
- ELGHOBASHI, S. E. & PUN, W. M. 1974 A theoretical and experimental study of turbulent diffusion flames in cylindrical furnaces. *Proceedings of Fourteenth International Symposium on Combustion* .
- HAMINS, A., THRIDANDAM, H. & SESHADRI, K. 1985 Structure and extinction of a counterflow partially premixed, diffusion flame. *Chemical Engineering Science* **40**, 2027–38.
- HAMLINGTON, P.E., POLUDNENKO, A. Y. & ORAN, E. S. 2010 Turbulence and scalar gradient dynamics in premixed reacting flows. *40th AIAA Fluid Dynamics Conference* **2010 5027**, 2285–2306.
- HAMLINGTON, P. E., SCHUMACHER, J. & DAHM, W. J. A. 2008 Local and nonlocal strain rate field and vorticity alignment in turbulent flows. *Physical Review E* **77**, 026303–1–8.
- HELLWIG, W., SHI, X. & SIRIGNANO, W. A. 2023a Three-dimensional vorticity effects on extinction behavior of laminar flamelets. in *journal review, arXiv[2307.03695]* .

- HELLWIG, W., SHI, X. & SIRIGNANO, W. A. 2023*b* Vortex stretching of non-premixed, diluted hydrogen/oxygen flamelets. *in journal review, arXiv[2402.03615]* .
- JOHNSON, P. 2021 On the role of vorticity stretching and strain self-amplification in the turbulence energy cascade. *Journal of Fluid Mechanics* **922**, A3–1–35.
- JOHNSON, P. & WILCZEK, M. 2023 Multiscale velocity gradients in turbulence. *Annual Review of Fluid Mechanics* **56**, 463–90.
- JONES, W. P. & LAUNDER, B. E. 1972 The prediction of laminarization with a two-equation model of turbulence. *International Journal of Heat and Mass Transfer* **15**, 301–14.
- KARAGOZIAN, A. R. & MARBLE, F. E. 1986 Study of a diffusion flame in a stretched vortex. *Combustion Science and Technology* **45**, 65–84.
- LIÑÁN, A. 1974 The asymptotic structure of counterflow diffusion flames for large activation energies. *Acta Astronautica* **1**, 1007–39.
- LÓPEZ-CÁMARA, CLAUDIA-F., JORDÀ JUANÓS, ALBERT & SIRIGNANO, WILLIAM A. 2020 Strain rate and pressure effects on multi-branched counterflow flames. *Combustion and Flame* **221**, 256–69.
- MARBLE, F. E. 1985 Growth of a diffusion flame in the field of a vortex. In *Recent Advances in the Aerospace Sciences*, pp. 395–413. Plenum Press, New York.
- NOMURA, K. K. & ELGHOBASHI, S. E. 1992 Mixing characteristics of an inhomogeneous scalar in isotropic and homogeneous sheared turbulence. *Physics of Fluids A* **4**, 606–25.
- NOMURA, K. K. & ELGHOBASHI, S. E. 1993 The structure of inhomogeneous turbulence scalar in variable density nonpremixed flames. *Theoretical and Computational Fluid Dynamics* **5**, 153–75.
- PETERS, N. 1984 Laminar diffusion flamelet models in non-premixed turbulent combustion. *Progress in Energy and Combustion Science* **10**, 319–339.
- PETERS, N. 2000 *Turbulent Combustion*, 1st edn. Cambridge, UK: Cambridge University Press.

- PIERCE, C.D. & MOIN, P. 2004 Progress-variable approach for large-eddy simulation of non-premixed turbulent combustion. *Journal of Fluid Mechanics* **504**, 73–97.
- PITSCH, H. 2022 Flamemaster, a c++ computer program for 0d combustion and 1d laminar flame calculations. version v4.2.1.
- POPE, S. B. 2000 *Turbulent Flows*. Cambridge University Press.
- RAJAMANICKAM, P., COENEN, W., SANCHEZ, A. L. & WILLIAMS, F. A. 2019 Influences of stoichiometry on steadily propagating triple flames in counterflows. *Proceedings of the Combustion Institute* **37**, 1971–7.
- ROBINSON, A. C. & SAFFMAN, P. G. 1984 Stability and structure of stretched vortices. *Studies in Applied Mathematics* .
- ROTT, NICHOLAS 1958 On the viscous core of a line vortex. *Zeitschrift für angewandte Mathematik und Physik* **IXb**, 543–553.
- SIRIGNANO, W. A. 2019 Counterflow and wall stagnation flow with three-dimensional strain. *Physics of Fluids* **31**, 053605 <https://doi.org/10.1063/1.5096472>.
- SIRIGNANO, W. A. 2021a Combustion with multiple flames under high strain rates. *Combustion Science and Technology* **192**, 1173–1202.
- SIRIGNANO, W. A. 2021b Mixing and combustion in a laminar shear layer with imposed counterflow. *Journal of Fluid Mechanics* **908**, 1–33A35.
- SIRIGNANO, W. A. 2022a Inward swirling flamelet model. *Combustion Theory and Modelling* **26**, 6, 1014–40.
- SIRIGNANO, W. A. 2022b Stretched vortex layer flamelet. *Combustion and Flame* **224**, 112276.
- SIRIGNANO, W. A. 2022c Three-dimensional, rotational flamelet closure model with two-way coupling. *Journal of Fluid Mechanics* **945**, A21.
- SMITH, G.P., TAO, Y. & WANG, H. 2016 Foundational fuel chemistry model version 1.0 (ffcm-1).

- STEINBERG, A. M. & DRISCOLL, J. F. 2009 Straining and wrinkling processes during turbulence-premixed flame interaction measured using temporally-resolved diagnostics. *Combustion and Flame* **156**, 2285–2306.
- STEINBERG, A. M., HAMLINGTON, P.E. & ZHAO, X. 2021 Structure and dynamics of highly turbulent premixed combustion. *Progress in Energy and Combustion Science* **85**, 100900.
- SWAMINATHAN, N. & GROUT, R. W. 2006 Interaction of turbulence and scalarfields in premixed flames. *Physics of Fluids* **18**, 045102.
- TAO, YUJIE, SMITH, GREGORY P. & WANG, HAI 2018 Critical kinetic uncertainties in modeling hydrogen/carbon monoxide, methane, methanol, formaldehyde, and ethylene combustion. *Combustion and Flame* **195**, 18–29, special Commemorative Issue: Professor Chung King (Ed) Law 70th Birthday.
- WALSH, SYLVAIN L., ZHAN, LEI, MEHRING, CARSTEN, LIU, FENG & SIRIGNANO, W. A. 2024 Turbulent accelerating combusting flows with a methane-vitiated air flamelet model. *AIAA Journal* . In journal review.
- WILLIAMS, F. A. 1975 Recent advances in theoretical descriptions of turbulent diffusion flames. In *Turbulent Mixing in Nonreactive and Reactive Flows*, Editor S. N. B. Murthy, pp. 189–208. Springer.
- WILLIAMS, F. A 2000 Progress in knowledge of flamelet structure and extinction. *Progress in Energy and Combustion Science* **26**, 657–82.
- YEUNG, P. K., DONZIS, D.A. & SREENIVASAN, K.R. 2012 Dissipation, enstrophy and pressure statistics in turbulence simulations at high reynolds numbers. *Journal of Fluid Mechanics* **700**, 5–15.